OBS noise reduction from horizontal and vertical components using harmonic-percussive separation algorithms

Zahra Zali[1,2], Theresa Rein[1], Frank Krüger[1], Matthias Ohrnberger[1], Frank Scherbaum[1]

[1]University of Potsdam, Institute of Geosciences, Karl-Liebknecht-Str. 24-25, 14476 Potsdam, Germany

[2]GFZ German Research Centre for Geosciences, Potsdam, Germany

Correspondence to: Zahra Zali (zali@uni-potsdam.de)

Zahra Zali: Campus Golm, Building 29, Room 2.48, Karl-Liebknecht-Str. 24-25, 14476 Potsdam, Germany

(zali@uni-potsdam.de)

Theresa Rein: Campus Golm, Building 27, Room 0.43, Karl-Liebknecht-Str. 24-25, 14476 Potsdam,

Germany (theresa.rein@uni-potsdam.de)

Frank Krüger: Campus Golm, Building 27, Room 1.36, Karl-Liebknecht-Str. 24-25, 14476 Potsdam,

Germany (Frank.Krueger@geo.uni-potsdam.de)

Matthias Ohrnberger: Campus Golm, Building 27, Room 1.37, Karl-Liebknecht-Str. 24-25, 14476

Potsdam, Germany (Matthias.Ohrnberger@geo.uni-potsdam.de)

Frank Scherbaum: Campus Golm, Building 29, Room 1.52, Karl-Liebknecht-Str. 24-25, 14476 Potsdam,

Germany (Frank.Scherbaum@geo.uni-potsdam.de)

Abstract

Records from ocean bottom seismometers (OBS) are highly contaminated by noise, which is much stronger compared to data from most land stations, especially on the horizontal components. As a consequence, the high energy of the oceanic noise at frequencies below 1 Hz considerably complicates the analysis of the teleseismic earthquake signals recorded by OBSs.

Previous studies suggested different approaches to remove low-frequency noises from OBS recordings, but mainly focused on the vertical component. The records of horizontal components, crucial for the application of many methods in passive seismological analysis of body and surface waves, could not be much improved in the teleseismic frequency band. Here we introduce a noise reduction method, which is derived from the harmonic-percussive separation algorithms used in Zali et al., (2021) in order to separate long-lasting narrowband signals from broadband transients in the OBS signal. This leads to significant noise reduction of OBS records on both the vertical and horizontal components and increases the earthquake signal-to-noise ratio (SNR) without distortion of the broadband earthquake waveforms. This is demonstrated through tests with synthetic data. Both SNR and cross-correlation coefficients showed significant improvements for different realistic noise realizations. The application of denoised signals in surface wave analysis and receiver functions is discussed through tests with synthetic and real data.

1 Introduction

Ocean bottom seismometer recordings are generally difficult to analyze, because the noise level is usually much higher compared to land stations. At frequencies below 1 Hz, the effect of the ocean noise is often dominating the data and hinders the seismological analysis (e.g. Webb et al., 1991; Crawford, 1994). Signals of interest, i.e. transient signals, especially from teleseismic events can be masked by the oceanic noise. Here, the horizontal components are most strongly contaminated by low frequency noise. To illustrate the noise on OBS data, we exemplary show the records of the station D10 of the DOCTAR array (see Fig. 1 and Fig. S1). Various studies tried to identify and characterize the different sources of noise recorded at the ocean bottom (e.g. Webb, 1998; Crawford & Webb, 2000; Corela, 2014; Stähler et al., 2018; Essing et al., 2021; An et al., 2021). In our study, we focus on noise sources that especially affect teleseismic horizontal recordings in the frequency band of 0.02–2 Hz. Generally, the dominant natural noise signals in the oceanic environment are secondary oceanic microseisms (Rayleigh/Scholte waves at the ocean bottom) caused by the interaction of wind-generated water waves, infragravity waves (compliance noise) as well as tilt noise; the latter is originating from the turbulent interaction between currents and the instrument (e.g. Crawford et al., 1998; Corela, 2014). Primary oceanic microseism is originating from the interaction of water waves incident at steep coastlines and/or rough seafloor (Hasselmann, 1963; Webb, 1998; Bell et al., 2015). Its spectral peak is around 0.07 Hz (Friedrich et al. 1998) in the Northern Atlantic. The secondary microseism has frequencies above 0.1–0.25 Hz, with a highest spectral peak around 0.14 Hz (Friedrich et al., 1998, Fig. 1). It is caused by wind or swell waves propagating in opposite directions. The primary and secondary microseisms affect both the vertical and

57 horizontal seismometer components, whereas the compliance noise is solely observed on the vertical
58 component and the hydrophone. Compliance noise, dominant in the frequency band of 0.01–0.04 Hz, is
59 only significant if its wavelength exceeds the water depth (Crawford et al., 1998; Crawford & Webb, 2000;
60 Bell et al., 2015).

61 Below frequencies of 0.01 Hz and 0.1 Hz, the vertical and especially the horizontal components, are highly
62 contaminated by tilt noise generated by ocean bottom currents (Webb, 1998; Crawford& Webb, 2000;
63 Stähler et al., 2018, Fig. 1). The tilt noise level increases with signal period (see Fig. 1). The ocean bottom
64 currents in many regions of the oceans are mostly driven by tidal force and often create a signal with
65 strongest amplitudes below 1 Hz, appearing every 6–12 hours (e.g. Brink, 1995; Crawford & Webb, 2000;
66 Ramakrushana Reddy et al., 2020; Essing et al., 2021). The ocean bottom currents passing the instrument
67 create local eddy currents, deform the seafloor beneath the sensor and tilt the whole instrument frame, to
68 which the seismometer is fixed (e.g. Duennebier & Sutton, 1995; Webb, 1998; Romanowicz et al., 1998;
69 Crawford & Webb, 2000; Corela, 2014; Stähler et al., 2018). If the seismometer mass is not perfectly
70 leveled, the high tilt noise on the horizontal components is partially projected onto the vertical component
71 (e.g. Crawford, 1994; Corela, 2014; Bell et al., 2015). Since the noise sources often act at frequencies of
72 teleseismic earthquakes, it is crucial to improve the signal-to-noise ratio (SNR) on OBS recordings for the
73 analysis of the Earth's crustal and mantle structure. Various studies discussed the improvement of OBS
74 recordings through different approaches, either by suggesting a better OBS instrument design (Stähler et
75 al., 2018, Corela, 2014, Essing et al., 2021), or by removing significant amounts of the noise from the
76 contaminated data by signal processing (Crawford & Webb, 2000, Bell et al., 2015, Janiszewski et al.,
77 2019). Our study follows the latter approach.

78 Crawford and Webb (2000) developed a method to remove noise from the vertical OBS component.
79 Calculating the linear transfer function between the horizontal and the vertical component allows
80 estimating the tilt noise which then can be subtracted from the vertical component. Hydrophone data
81 measured in parallel to the seismometer recordings allow reducing the influence of infragravity waves on
82 the vertical seismometer component recordings. For better results, Bell et al. (2015) propose to first rotate
83 the horizontal components into the direction of the highest coherence between the horizontal and vertical
84 component before calculating the linear transfer functions. The mentioned methods solely improve the
85 SNR on the vertical component whereas the noise contamination on horizontal components is often larger.
86 Other recent studies attempted to reduce noise also on the horizontal components (Mousavi and Langston,
87 2017; Zhu et al., 2019; An et al., 2021; Negi et al., 2021). An et al. (2021) tried to reduce the noise on the
88 horizontal components by applying the reversed procedure of Bell et al. (2015). Rotation of one horizontal
89 component into the direction of the principle noise indeed results in an improvement of the orthogonal
90 horizontal component, but the other horizontal component became noisier (An et al., 2021). Results of a
91 recent study applying a polarization filter to reduce the noise on all components show strong changes of the
92 broadband waveforms (Negi et al., 2021). The automatic noise-attenuation method developed by Mousavi
93 and Langston (2017) is a time-frequency denoising algorithm using the wavelet transform and

94 synchrosqueezing. It can be either used to keep the signal and remove the noise or vice versa. The
95 decomposition method DeepDenoiser from Zhu et al. (2019) is based on a deep neural network.
96 DeepDenoise decomposes the waveform into signal and noise in the time-frequency domain. The latter
97 methods, both improve the SNR, but mainly focus on local and regional earthquake detection. They result
98 in changes in the waveform shape if the noise amplitude directly ahead of the signal is significant in
99 comparison to the signal amplitude in a specific frequency. However, the analysis of undistorted broadband
100 waveforms on the horizontal components is crucial for many passive seismological structure analysis
101 methods, e.g. the calculation of receiver functions or surface wave dispersion and polarization analysis.

102 Here we introduce a method, inspired from the music information retrieval (MIR) research, which is
103 adapted to seismological data and is used for noise reduction on both, the vertical and the horizontal
104 components.

105 Seismic waveforms and acoustic signals generated by musical instruments are similar in some aspects
106 (Schlindwein et al., 1995; Johnson and Watson, 2019). The extensive research in the field of music
107 information retrieval has resulted in advances (e.g., Müller, 2015) that may be useful in seismic signal
108 processing as well. Exploiting the idea of harmonic-percussive separation (HPS) in MIR, Zali et al. (2021)
109 developed an algorithm to separate harmonic volcanic tremor from earthquakes in seismic waveforms. In
110 the present study we use this algorithm after some modifications in order to separate 'harmonic' (long-
111 lasting narrowband signals) and 'percussive' (broadband transients) components of an OBS data set aiming
112 at noise reduction and retrieval of clearer broadband earthquake waveforms. Throughout this study we will
113 make use of the term noise for any signal other than earthquake signal in the data set. In the context of OBS
114 noise reduction using HPS algorithms, percussive components correspond to earthquake signals and
115 harmonic components correspond to noise signals. The long-duration OBS noise signals that last a few
116 hours to days (depending on the noise type) with a restricted frequency range contrasts with transient
117 seismic signals such as earthquakes with a wider range of frequencies.

118 The algorithm introduced in Zali et al., (2021) is a combination of two HPS approaches that leads to the
119 desired signal separation. Here we also use the two approaches subsequently in order to separate different
120 type of noise signals from the earthquake signals. In the first step we adopt HPS using a similarity matrix
121 (Rafii and Pardo, 2012; Rafii et al., 2014) to separate monochromatic and harmonic noises. In the second
122 step we adopt HPS using median filtering (FitzGerald, 2012) in order to separate the remaining narrow-
123 band signals. With this two-step approach we can separate and remove much of the OBS noise
124 contamination from the earthquake signals.

125

126 **2 Data**

127 In this study we discuss the noise recorded by a LOBSTER (Longterm OBS for Tsunami and Earthquake
128 Research) OBS instrument from the DEPAS pool, which is equipped with a Güralp CMG-40T
129 seismometer, a MCS (Marine compact seismic) recorder and loose cables (for technical specification see
130 Stähler et al., 2018). We show data recorded during the DOCTAR deployment, using DEPAS-LOBSTERs,

131 located around the Gloria Fault in the Northern Atlantic. Twelve DEPAS-LOBSTERs form the array. They

132 were deployed between 2011-2012 and recorded the data with a sampling frequency of 100 Hz

133 (Hannemann et al., 2016; Hannemann et al., 2017).

134 Until 2019 the DEPAS LOBSTER OBS was built with an OBS-specific version of the Güralp CMG-

135 40T/MCS recorder, where the seismometer had a corner frequency of 60 s and has been modified to last

136 long on the seafloor (Stähler et al., 2018). However, the development of less power consumption lead to a

137 higher noise level of the instrument itself (Stähler et al., 2018). At low frequencies (<0.1 Hz) the self-noise

138 of the sensor is highly affecting the records, especially on the vertical component. However, the design of

139 the DEPAS-LOBSTERs has been improved for deployments after 2019 (e.g. Essing et al., 2021).

140 We observed a continuous harmonic signal at a frequency of 0.04 Hz, partially with one or two overtones

141 on a subset of the array (see Fig. 1). This signal was observed on 30% of the stations from the DOCTAR

142 project (e.g., Hannemann et al, 2016, Hannemann et al., 2017) and on 43% of the stations from the

143 KNIPAS project (Schlindwein et al., 2018), both using the mentioned DEPAS-LOBSTER design. We

144 cannot identify the source of this signal yet, but based on its continuity, we assume an electronic source

145 from the instrument itself.

146 The hydrophone and especially the horizontal components are highly affected by the strumming of the

147 head-buoy, which is attached to the DEPAS-LOBSTER frame causing a 'current-induced harmonic tremor

148 signal' (Stähler et al., 2018; Essing et al., 2021, Fig. 1). These 'tremor events' last over up to 4 hours and

149 appear every 6–12 hours. These presumably tidal-driven tremor events are harmonic signals with a

150 fundamental period of 0.4–1 s and various overtones (1–10 Hz) (Stähler et al., 2018; Essing et al., 2021,

151 Fig. 1). Regarding the frequency band, 'tremor events' mainly affect the analysis of teleseismic body

152 waves, especially on the horizontal component (Fig. 1).

153

154 **3 Noise reduction methodology**

155

156 **3.1 Harmonic-percussive separation (HPS)**

157

158 Harmonic-percussive separation refers to the problem of decomposing a signal into its harmonic and

159 percussive components. This topic has received much attention in recent years (Rafii et al., 2018) and has

160 numerous applications in the field of MIR and musical signal processing.

161

162 Within a general context harmonic signals show an overtone structure in the spectral domain. We call

163 overtones one or more clear narrow-banded frequency peaks being integer multiples of the fundamental

164 frequency (the first frequency peak in the spectrum). Harmonic signals have a relatively stable behavior

165 over time and can be identified in a Short Time Fourier Transform (STFT) spectrogram by horizontal
166 structures referred to constant frequencies along the time axis.

167 In contrast, percussive signals form vertical structures in a STFT spectrogram that contain energy in a wide
168 range of frequencies. Therefore it is a straightforward strategy in most HPS algorithms to try to separate the
169 horizontal structure from the vertical structure in the spectrogram corresponding to harmonic and
170 percussive components, respectively. The horizontal lines in the spectrogram could correspond to either
171 harmonic signals or monochromatic signals.

172

173 OBS noise forms narrowband horizontal structures in the STFT spectrogram while earthquake signals have
174 vertical exhibition in the STFT spectrogram.

175

176 **3.2 HPS using median filtering (MED)**

177

178 In the context of HPS, one of the simplest and fastest approaches is median filtering (FitzGerald, 2010). For
179 simplification we name this algorithm as MED in this study. Median filters are usually used to remove
180 noise from an image or a signal. Using a median filter a sample will be replaced by the median of
181 neighboring samples within a window of a specific length (The specific length is the kernel size of the
182 median filter). The entire signal is processed using a sliding window analysis. Within the HPS, two median
183 filters are applied to the amplitude of the STFT spectrogram of a signal. One median filter is performed
184 along the time axis of the spectrogram to suppress percussive events and enhance harmonic components.
185 Another median filter is applied along the frequency axis in order to enhance percussive events and
186 suppress harmonic components. The two resulting spectrograms are then subsequently used to create two
187 masks, which are applied to the original signal spectrogram separately to generate two spectrograms of
188 harmonic and percussive components, respectively. For creating the harmonic and percussive signals in the
189 time domain the phase of the original signal is added to each spectrogram and the time domain signals are
190 reconstructed using the inverse STFT.

191

192 **3.3 HPS using the similarity matrix (SIM)**

193

194 Another powerful approach in HPS proposed by Rafii & Pardo (2012) is based on calculating a similarity
195 matrix. We name this algorithm as SIM here. This approach is a repetition-based separation, which
196 identifies repeating elements in the spectrogram by looking for similarities by means of a similarity matrix.
197 Within the SIM algorithm, first similar time frames in the spectrogram are identified through a similarity
198 matrix. Then a median filter is applied only to the frames identified as similar to constitute the repeating
199 spectrogram model that corresponds to harmonic components. The non-repeating spectrogram that
200 corresponds to the percussive component of the data is obtained by subtracting the repeating spectrogram
201 from the original spectrogram. For creating the repeating and nonrepeating signals in the time domain, the

202 phase of the original signal is added to each spectrogram and the time domain signals are reconstructed
203 using the inverse STFT. Details of this approach are discussed in the following section.
204

205 **3.4 HPS noise reduction algorithm for OBS data**

206

207 The motivation for using HPS for noise reduction of OBS data stems from the different characteristic of
208 earthquake and OBS noise signals as described in Sect. 2. Earthquakes are broadband transient signals,
209 while the signals of OBS noises are more narrow-band compared to earthquakes. We combine two
210 modified HPS algorithms to separate those signals in a two-step procedure. We divide the frequency
211 content of the signal into two frequency ranges; range one covers the frequency range between 0.1 to 1 Hz
212 whereas range two contains the complementary frequency range, i.e. all frequencies except the band
213 between 0.1 and 1 Hz. Then two different algorithms are applied to range one and range two, respectively.
214 In the first step, we use the SIM algorithm and separate only harmonic or monochromatic signals from the
215 original records in range two avoiding the frequency range of 0.1 to 1 Hz. The reason is related to the
216 frequency content of the noise and earthquake signals and how the SIM algorithm separates them. For a
217 better understanding, we first explain how the algorithm works and then present more detail about this
218 selection. In the second step, to reduce noise from the specified frequency range we apply MED. There we
219 target harmonic (or monochromatic) as well as narrow-band signals with gliding frequencies named as
220 current-induced harmonic tremor signal in the Sect. 2. The overall schematic diagram of our HPS noise
221 reduction algorithm along with an example is shown in Fig. 2.
222 The SIM algorithm is explained in the following: From the original OBS record SO (SO represents the
223 original restituted OBS signal) we derive the STFT named X being a complex-valued spectrogram.
224 The complex-valued spectrogram **X** is separated into its amplitude and phase components using Eq. 1.
225

$$X = V * exp(1j * \varphi), \qquad (1)$$

226

227 where φ is the phase of **X**, $V = |X|$ is the amplitude of X and j is the imaginary unit.
228 All of the spectrogram modifications will be applied to the amplitude spectrogram **V**. The cosine similarity
229 (the similarity between two vectors of an inner product space) between the STFT time frames is calculated
230 through the multiplication of the transposed **V** by **V** with the normalization of the **V**. This is shown in Eq.
231 2.
232

$$S(k_a, k_b) = \frac{\sum_{i=1}^{n} V(i, k_a) V(i, k_b)}{\sqrt{\sum_{i=1}^{n} V(i, k_a)^2} \sqrt{\sum_{i=1}^{n} V(i, k_b)^2}}, \qquad (2)$$

233

7

234 where **S** is the similarity matrix. Each point (k_a, k_b) in **S** is the cosine similarity between time frame k_a

235 and k_b of **V**, $\forall k_{a,b} \in [1,\text{m}]$, where m is the number of time frames and n is the number of frequency

236 channels for each time frame. Once the similarity matrix is calculated we use it to determine the most

237 similar time frames to each single time frame. For time frame k_a we compare all the values in $S(k_a, \text{k}_i)$

238 for i$\in$ [1,m]. We identify similar frames for time frame k_a, by choosing the upper 2% of the all time

239 frames with the highest similarities.

240 Finally, all similar time frames to any frame k in **V** are stored in a temporary array **K**. Those similar time

241 frames are used to create a repeating spectrogram model **W**. The corresponding frame in **W** is obtained by

242 taking the median of **K** for each frequency at each time frame k. Those time-frequency bins, which are

243 similar with little deviations between repeating frames, are captured by the median and constitute the

244 repeating spectrogram model. This spectrogram contains only similar and repeating patterns. The time-

245 frequency bins with large deviations between repeating frames would constitute nonrepeating transient

246 patterns and would be suppressed by median filtering.

247

248 The nonnegative spectrogram **V** is the sum of two nonnegative spectrograms of repeating and nonrepeating

249 patterns, hence, **W** (the repeating spectrogram model) should always have smaller values or at most be

250 equal compared to **V**. To ensure this, a repeating spectrogram model $\widetilde{\mathbf{W}}$ is defined by taking the minimum

251 between **W** and **V**. The nonrepeating spectrogram model is derived by subtracting $\widetilde{\mathbf{W}}$ from **V**.

252

253 We use these two (the repeating and the nonrepeating) spectrogram models to create two time-frequency

254 masks for repeating and nonrepeating patterns, respectively. Instead of the binary mask, which is used in

255 Rafii & Pardo (2012), we use soft masks via Wiener filtering (Vaseghi, 1996). The calculation of the soft

256 masks is shown in the following equations:

257

$$M1 = \frac{\widetilde{W}^2}{\widetilde{W}^2 + \left(V - \widetilde{W}\right)^2}\text{''} \qquad (3)$$

$$M2 = \frac{\left(V - \widetilde{W}\right)^2}{\left(V - \widetilde{W}\right)^2 + \widetilde{W}^2}\text{,} \qquad (4)$$

258

259

260 in which **M1** and **M2** are repeating and nonrepeating masks respectively. We multiply the masks with the

261 input amplitude spectrogram **V** to separate the repeating and nonrepeating components. The element-wise

262 multiplication of the masks by the input amplitude spectrogram **V** is shown in the following equations:

263

8

$$R = M1 \otimes V, \tag{5}$$

$$NR = M2 \otimes V, \tag{6}$$

264

265   in which **R** and **NR** denote repeating and nonrepeating amplitude spectrograms respectively.

266

267   The resulting **R** and **NR** spectrograms are shown in Fig. 2a for a specific/typical example of an OBS
268   recording. As can be observed in the **R** spectrogram, in particular the low frequency harmonic or
269   monochromatic signals below 0.1 Hz are well captured. We applied the SIM algorithm only to the
270   frequency band below 0.1 Hz and above 1 Hz. In the frequency band from 0.1 Hz to 1 Hz the signals
271   remain unchanged by this procedure. This is the first constraint we consider for the SIM algorithm. In the
272   field of noise reduction using signal processing techniques, a very important point is to not modify the
273   signals of interest for analysis. P and S waveforms in the teleseismic earthquake signals have often
274   frequency content in the range of 0.1 Hz to 1 Hz with a dominant frequency around 0.3 Hz. Oceanic
275   microseism noise, which is usually present in the OBS data, has a dominant frequency around 0.1 Hz to 0.3
276   Hz. As P and S phases have similar dominant frequency as the microseism noise wavefield, superposition
277   of both wavefields could happen in this frequency range. They could interfere constructively or
278   destructively so the resulting amplitude could be higher or lower compared to the original P or S phase
279   amplitudes. Considering these interferences, using the SIM algorithm, may result in creating fake higher
280   amplitude for these phases or losing part of their amplitude in the noise reduced signal. But this could be
281   problematic only when the amplitude of the noise is changing over the time. For a noise signal with almost
282   constant amplitude, the SIM algorithm can extract the true amplitude of the noise even in the interference
283   moments. However, the microseism noise has slightly varying amplitude over time.

284

285   Before moving to the second step we introduce a second constraint parameter, which we use in the SIM
286   algorithm. Surface waves of teleseismic events show usually a dispersed narrow-band signal and
287   correspond to mainly horizontal patterns of short duration (on a daily scale) in the spectrogram. Given the
288   way the HPS is separating harmonic from transient signals, the surface wavetrain may be erroneously
289   recognized as harmonic component and thus be separated as noise signal. In order to prevent this and
290   preserve the whole frequency content of the earthquake, we define a so-called waiting factor for the
291   similarity calculation introducing a minimum time distance between two consecutive similar frames. For
292   the problem of retaining teleseismic surface waves we found that a waiting time of at least two hours
293   prevents the algorithm to prune surface waves from the transient signal part. The rationale is that the
294   duration of a teleseismic event is usually less than two hours whereas the noise components have longer
295   duration. Using this waiting factor prevents separating any harmonic component of the earthquake signal as
296   noise component. As a side effect this constraint causes that short-duration harmonic/monochromatic noise
297   signals won't be well captured, too. However, these types of signals are not common in OBS data (see the

298   Sect. 2).

299

300   In the second step of our algorithm, to target noise signals in the frequency range of 0.1 Hz to 1 Hz, we use

301   MED as it is described in the Sect. 3.2. We apply this second part of the noise removal procedure only to a

302   restricted frequency band of 0.1 Hz to 1 Hz. The dominant noise in the mentioned frequency range is the

303   current-induced harmonic tremor signal (see the Sect. 2).

304   First we create the $\mathbf{X'}$ spectrogram which is equal to $\mathbf{X}$ in the mentioned frequency range and is equal to

305   zero outside of this band. Then we apply a horizontal median filter to $\mathbf{X'}$ in order to separate harmonic

306   components. This results in the harmonic spectrogram $\mathbf{H,}$ which contains near-horizontal patterns captured

307   by the median filter.

308   Now we have two separated spectrograms for noise signals: $\mathbf{R}$, which is derived from the first step, and $\mathbf{H}$,

309   which is derived from the second step. Summing these two spectrograms will build the noise spectrogram

310    $\mathbf{N}$. Subtracting $\mathbf{N}$ from the input amplitude spectrogram $\mathbf{V}$ will construct the transient spectrogram $\mathbf{T}$.

311   As can be seen in Fig. 2a in step 2, the dominant energy of the narrow-band signals with gliding

312   frequencies in the range of 0.1 Hz to 1 Hz (the current-induced harmonic tremor noise as introduced in the

313   Sect. 2) is captured in the noise spectrogram $\mathbf{N}$, but part of it remains in the transient spectrogram $\mathbf{T}$.

314   Signals with changing frequency which don't form complete horizontal lines in the spectrogram, are

315   difficult to capture by our HPS algorithm, so part of their energy remains in the final spectrogram.

316

317   **3.5 Reconstruction of the denoised signal**

318   In order to reconstruct the noise-removed signal in the time domain we must add phase information to the

319   spectrogram. We had separated the complex-valued spectrogram $\mathbf{X}$ into its amplitude $\mathbf{V}$ and its phase

320   component using Eq. 1 and all the further modifications have been applied to the amplitude spectrogram $\mathbf{V}$.

321   The phase of input signal SO is mostly affected by the phase of noise signals as they have the dominant

322   energy in the signal. Therefore, we use the phase information of SO in order to reconstruct the noise signal.

323   We add this phase to the noise spectrogram $\mathbf{N}$ using the following equation:

324

$$N' = N * exp(1j * \varphi), \qquad\qquad (7)$$

325

326   where N' is the complex-valued noise spectrogram. We reconstruct the noise signal *NS* from the complex

327   spectrogram N', using the inverse STFT. Finally the OBS denoised signal HPS (HPS here represents the

328   SO signal after the HPS processing) is obtained by subtracting the noise signal from the input OBS signal

329   SO using the following equation:

330

10

$$HPS = SO - NS, \qquad (8)$$

331

332   **3.6 Parameters selection**

333

334   Many typical noise signals observed in OBS recordings are harmonic, monochromatic or narrow-band

335   signals with gliding frequencies (see the Sect. 2). In order to extract the expected narrowband noise signals

336   from the STFT we require a high-frequency resolution in the spectral domain, therefore, making it

337   necessary to use sufficiently long time windows for the spectral analysis. Here we use an FFT window

338   length of 163.84 seconds with an overlap of 75%, corresponding to an FFT size of 16384 at a sampling

339   frequency of 100 Hz, which corresponds to a frequency resolution of 0.006 Hz.

340   We use a kernel size of 80 for the median filter in the MED algorithm. The larger the kernel size, the more

341   noise signal would be captured. However, using very large sizes could introduce waveform distortions. As

342   it is discussed in Driedger et al. (2021), the kernel size is not critical as far as not using extreme values. Our

343   tests show that a kernel size of 80 is the largest size, which leads to a safe separation without capturing any

344   energy of the teleseismic signal.

345   The values of parameters, which we used for this study, are presented in the Table 1. These are our

346   recommendations for noise reduction of teleseismic earthquakes. One can tune the parameters based on

347   other specific applications such as denoising local earthquakes or extracting specific signals like

348   microseism signal.

349

350   **4 Results and Discussion**

351

352   **4.1 General Results**

353

354   In this section we aim to demonstrate the reliability of our HPS noise reduction algorithm and evaluate the

355   improvement of the OBS data. We applied the method to synthetic and real teleseismic earthquake data

356   recorded by the OBS station D10 of the DOCTAR array (e.g., Hannemann et al, 2016, Hannemann et al.,

357   2017). The synthetics were calculated for a source-receiver epicentral distance of 40° (focal depth: 45 km,

358   focal mechanism: double couple, source duration: 4 s) by using the full wavefield software qseis (Wang,

359   1999) and a modified average ak135 velocity model including a water layer (Kennett et al, 1995). The

360   crustal structure of the velocity model is adapted to the oceanic crust (crustal thickness is 6.6 km) in that

361   area and the water depth is fixed to 4.9 km. Real oceanic noise of the ZRT components recorded by the

362   station D10 is added to the corresponding components of the synthetic teleseismic signal. We created

363   synthetics for three different noise situations at the beginning (N1), during (N2) and after (N3) tidal

364   currents (Fig. 3) each with theoretical SNR of 1–10 between noise and P-onset on pure synthetic Z.

365   Throughout the whole paper the SNR is defined as root mean square (RMS) of the signal divided by RMS

366 of the noise. For further details of synthetic data creation see Fig. S2. For the comparison with real data, we

367 selected in total 46 teleseismic events with magnitudes Mw >5.6 and epicentral distances of 30–160° (see

368 Fig. S1). Here only those events were used, where a P onset could be visually identified. The pre-selection

369 of the events is taken from Hannemann et al. (2017) and expanded by some events with low magnitudes

370 (see Table S1). In the following, we will discuss the improvement of the records by comparing the

371 seismograms and spectrograms of synthetic and real data. We also illustrate the improvement for two

372 seismological applications (teleseismic surface wave group velocity analysis and receiver function

373 analysis). For some observations, e.g. checking the phase arrival of the teleseismic body waves, we rotated

374 the arbitrarily orientated horizontal components of the real data into the ZRT system. The orientation

375 angles are taken from the previous study on the DOCTAR array (Hannemann et al., 2016).

376

377 Comparing the spectrograms and waveforms of the synthetic example we see a significant improvement of

378 SNR in the HPS processed data set on all components (e.g. Fig. 3 and Fig. S3–5 for the real data). The

379 continuous spectral lines of the assumed electronic noise are removed from the data, as well as most of the

380 spectral lines related to tremor episodes of head-buoy strumming. During the tides, we observe a reduction

381 of the spectral amplitudes for the tilt noise, as well as for the general background noise (Fig. 3 and Fig. S3–

382 5) on the horizontal components. The results concluded from the spectrograms are confirmed by the spectra

383 (Fig. 2b), which show the removal of the spectral peaks of the electronic noise (0.05, 0.1, 0.15 Hz) and the

384 tremor episodes (0.5–1 Hz). The whole amplitude and the phase information of the synthetic earthquake are

385 preserved in the HPS signal (see Fig. 3).

386 To quantify the improvements obtained when using our method, we calculated the cross-correlation of

387 the teleseismic waveform, the SNR of the teleseismic body-wave phases and the RMS of the teleseismic

388 waveform before and after denoising. Because most of the oceanic noise ranges at frequencies below 1 Hz,

389 which is also the most interested frequency range of the OBS analysis, a 1 Hz low pass filter is applied to

390 the signals before all result calculations.

391 We calculated the correlation coefficient for synthetic SO and HPS compared with the synthetic earthquake

392 signal for different SNR and noise realizations and plotted it in Fig. 4a. The high correlation coefficients for

393 HPS and synthetic compared with SO and synthetic in all cases demonstrate a significant noise reduction.

394 Furthermore, it is an indication that the HPS denoising preserves the earthquake signal and doesn't

395 introduce significant waveform distortions since the HPS is more similar to the synthetics compared to SO.

396 In the following we show other measures that confirm the preservation of the earthquake signal.

397 For the SNR calculation we used a signal window of 30 s starting from the theoretical onset (direct P on Z

398 component, direct S on R and T component and Love wave on the T component) and a noise window of 60

399 s starting 70 s before the theoretical onset. For the Love wave, the SV phase (R component) and P phase (Z

400 component) the SNR increased significantly (Fig. 4b). We find that the noise type properties influence the

401 perceived SNR improvement. It appears that there is no SNR improvement on the T-component for Noise

402 situation N1 (Fig. 4b, the second panel). N1 is taken from the tidal current event's beginning, where there is

12

403   a significant variation in noise-frequencies over time. In this instance, the signal and noise have comparable

404   frequency ranges. Despite the SNR showing no increase, a visual check of the matching trace reveals a

405   definite improvement in the waveform for the SH-wave on the T component. The results from the cross-

406   correlation (Fig. 4a), confirm the improvement and preservation of the waveform. The SNR should not be

407   utilized alone to assess the improvement by HPS noise reduction approach since we are concentrating on

408   the preservation of the waveform and the SNR comparison strongly depends on the noise situation. The

409   improvement of the traces by the HPS noise reduction approach is confirmed by the study of the cross-

410   correlations, RMS (which is explained in the following paragraph), and the pure waveforms, even though

411   the SNR is not improving in all instances.

412   The RMS amplitudes of a noise-free R component synthetic, SO and HPS signals are estimated over 8

413   seconds windows with 80% overlap and plotted in Fig. 4c. Comparing the RMS amplitude of the synthetic,

414   SO and HPS we see that the synthetic and HPS have similar amplitude ranges while SO has a much higher

415   amplitude. This shows a significant noise reduction in HPS along with preserving the energy of earthquake

416   and all the phase arrivals. As there is some noise remaining after denoising we see some differences in the

417   overall shapes of the RMS amplitude of the synthetic and HPS (especially after minute 24 which is almost

418   at the end of the energy of the synthetic signal). However, HPS shows peaks on the arrival times of seismic

419   phases of the synthetic which means that the energy of seismic phases is preserved after denoising. The

420   minor changes in seismic phase shapes of the synthetic and HPS are also due to the remaining noise. The

421   seismograms and spectrograms related to this example are presented in Fig. 3. Figure 4d shows a

422   comparison of RMS amplitude of the original noise in SO (blue curve), the remaining noise in HPS after

423   denoising (red curve) and the synthetic earthquake (green curve) signals. Besides a high noise reduction in

424   HPS, the plot shows that the remaining noise is independent of the pattern of the synthetic earthquake,

425   which confirms that the denoising process doesn't affect the earthquake energy in the HPS signal.

426

427   **4.2 Applications**

428   By applying our HPS noise reduction algorithm, we aim to improve seismological analyses, especially

429   those involving the analysis of teleseismic body and surface waves. Valuable constraints of the Earth's

430   structure in oceanic regions can be taken from the analysis of the SH-wavefield like Love-waves, which are

431   not influenced by the water column, but often cannot be analyzed due to strong noise on the horizontal

432   components. SV waves are also often masked by noise, but are for instance important for tomography

433   studies or S and SKS shear wave splitting analysis (e.g. Silver and Chan, 1991). Other techniques using the

434   SV-wavefield like the Z/R ratio of the teleseismic Rayleigh waves (Tanimoto & Rivera, 2008), or receiver

435   functions (RF) (Langston, 1979) also rely on clear radial component readings. In the following we will

436   show the improvement which was achieved for the SH arrivals and for the group velocity analysis of

437   teleseismic Rayleigh- and Love waves, as well as for the receiver function analysis.

438

439   **4.2.1 SH-waves**

440 Since SH-waves are weak in energy and displayed on the noise-contaminated transversal horizontal
441 component (T), they are sparsely observable on OBS recordings and are mostly masked by the high noise
442 level. However, on the HPS processed data we see an improvement of the SNR on the T-component (see
443 Fig. 4b). In many cases the SH-phase is clearly identifiable on the HPS T-component (see Fig. 3d for a
444 synthetic data and Fig. S6 for a real data example).

445

446 **4.2.2 Surface waves**
447 Rayleigh waves in deep oceanic domains are strongly influenced by the water column, because most of the
448 wave energy is traveling in the water. This poses a problem if the water depth changes along the travel
449 path. Love waves are not influenced by the water column but are recorded only on horizontal components
450 and their recordings on OBS systems are therefore more disturbed by strong noise sources like tilt-inducing
451 tidal currents. To test the performance of the HPS noise reduction algorithm in the long period range, we
452 performed a measurement of group velocities of Love and Rayleigh waves with the Multiple Filter
453 Technique (MFT) (Dziewonski et al., 1969). Figure 5 shows group velocity curves for the synthetic Love
454 wavetrain for the three noise situations N1-N3. For the MFT analysis we used the software mft96
455 (Herrmann, 2013). The unfiltered seismograms in the top panels (Fig. 5a–c) correspond to the P-wave SNR
456 = 1 scenario. In all three cases the clarity of the dispersion curve is greatly enhanced in the images resulting
457 from the HPS processed traces (Fig. 5e–g) in comparison to the noise free image (Fig. 5d). Also the
458 seismogram traces improved greatly. The dispersion maps show that also noise energy in the range of the
459 signal frequencies is removed successfully in the frequency range 0.05 to 0.2 Hz. Longer signal periods
460 which are weakly visible in the noise-free image (Fig. 5d) can not be recovered. The corresponding results
461 for the Rayleigh wavetrain on the radial component are shown in Fig. S7. For the N3 case here also longer
462 periods down to 40 s can be successfully denoised.
463 For an evaluation of the HPS denoising technique on real surface wave data we selected 23 events with
464 magnitudes larger than Mw 6.0 in the distance range between 47.5° and 159.6° and added one event with
465 Mw= 5.6 at a distance of 37.9° (see Fig. S1). Figure S8 shows seismograms and MFT analysis examples
466 for three events with different magnitudes and in different distances. The resulting group velocity
467 dispersion curves for all 24 events for the original and processed data are shown in Fig. S9. For all
468 components we find that the improved signal to noise ratio of the processed data allows the analysis of
469 more events and of a broader period range than in the original data.

470

471 **4.2.3 Receiver Functions**
472 Receiver functions have been proven to be a valuable tool to observe the Earth's structure using teleseismic
473 events (e.g., Langston, 1979, Ammon et al., 1995, Kind et al., 1995; Rondenay, 2009). Separating the
474 source site from the receiver site by deconvolution allows to estimate the Earth's structure beneath the
475 station. Here, we compare the receiver functions calculated from the synthetic examples and from real data
476 before and after denoising (Fig. 6). The synthetics used for the receiver function calculation are pure

14

477   synthetic signals contaminated by real noise (N1, N2, N3). On the synthetics, the SNR for P ranges

478   between 1–10 (for detailed description of the synthetic creation, see Sect. 4.1, Fig. 3 and S2). Receiver

479   function analysis and the observation of the Earth's structure beneath the DOCTAR array was already

480   calculated by Hannemann et al. (2017). Here, we don't aim to estimate the crustal and mantle structures,

481   instead we aim to compare the P-receiver Functions of the radial component calculated from the original

482   synthetic and real data (SO R-RF) with receiver functions of the radial component from the HPS processed

483   synthetic and real data (HPS R-RF). To calculate the receiver functions, we applied the iterative

484   deconvolution in the time domain (Ligorría & Ammon, 1999). We corrected the data for the Ps-phase,

485   quality controlled (e.g. P-onset at 0 s on Z of HPS R-RF), stacked and low-pass filtered the synthetic data at

486   2 Hz and bandpass filtered the traces between 0.05–0.5 Hz for the real data with a zero-phase Butterworth

487   filter. For both synthetic and real receiver function, the noise level strongly decreased and we observe a

488   significant decrease in variance on the HPS traces compared to the SO traces (Fig. 6).

489   Our result shows that determination of the crustal- and mantle-phases is more reliable on the HPS R-RF

490   stack than on the SO R-RF stack for both synthetic and real data (Fig. 6). We observe more distinct Ps-

491   phase arrivals on the HPS R-RF than on the SO R-RF stack. The Ps-phases are caused by the P-to-S

492   conversion at the Mohorovičić-, 410-km and 660-km discontinuity (hereafter referred to as Moho, 410, and

493   660, respectively; e.g. Deuss, 2009). For the synthetic example, we expect the P-to-s conversion at the

494   Moho at depths of 11.5 km to arrive at 0.8s, which is better resolved in the synthetic HPS R-RF than in the

495   synthetic SO R-RF, same for it's multiple (P_MsPp) and the water multiples every 6.5s (M_{WATER}, Fig. 6a).

496   Assuming ak135 velocities we would expect the $P_{410}s$-phase (Ps conversion at the 410) to arrive at around

497   43 s and the $P_{660}s$-phase (Ps conversion at the 660) at around 66.8 s delayed to the direct P-arrival (see Fig.

498   6 a & b).

499

500   Instead of a rather weak peak on the SO-R-RF real data stack we observe a strong peak at around 43 s, with

501   a good SNR on the HPS R-RF stack, indicating the sharp velocity contrast at the 410 (Fig. 6b). Comparing

502   SO-RF and HPS-RF real data stacks, the amplitudes of the P660s-phase on the HPS decreased and became

503   a broader peak. This aligns with our expectations from a conversion at a gradual velocity contrast as at the

504   660. These results are in line with the analysis of the crustal and mantle structure beneath the DOCTAR

505   array presented by Hannemann et al. (2017). The negative phase (X1 in Fig. 6b) arriving at around 5 s is

506   stronger on the HPS-R-RF real data stack than on the SO-R-RF real data stack and might either indicate the

507   PpSs multiple of the Ps-phase at the Moho, or the direct P-to-s conversion at the LAB. On the HPS-R-RF

508   real data stack we observe a strong positive phase (X2) arriving at 12 s (Fig. 6b). This phase has not been

509   identified by Hannemann et al. (2017) and a detailed analysis of its origin is beyond the scope of this study,

510   but it might be related to the water multiples.

511

512   **5 Conclusions**

513

514   In this work we have developed a method to separate the signals of teleseismic earthquakes from other
515   signals in OBS recordings resulting in noise reduction of OBS data. Our method is a combination of two
516   HPS algorithms from the field of MIR to separate harmonic and percussive components of OBS data.
517   Earthquake signals as percussive components are separated from noise signals as harmonic components.
518   The noise signal is reconstructed using the phase information of the original signal. Subtracting the noise
519   signal from the original signal derives the noise-reduced signal. Our two-step HPS approach results in a
520   cleaner, noise-reduced signal where the teleseismic broadband earthquake waveforms are preserved with
521   their whole frequency content. Our synthetic tests shows that the SNR of HPS noise reduced signal
522   significantly increases in most cases, however, the apparent SNR improvement depends on the noise type
523   characteristics. The type of noise signals, which are eligible for our noise reduction algorithm contains most
524   of the OBS noise energy.

525   The extracted noise signal contains some different signals where each can be derived by applying a band
526   pass filter to the extracted noise signal in a proper frequency band. The derived signal may be used in
527   researches related to that signal. For example the microseism signal can be extracted and used for
528   investigation of the source generation area of microseisms.

529   From our analysis of the broadband seismograms, we find out that the improvement is significant and
530   allows a broader and more reliable analysis of teleseismic earthquake data. Applications like the receiver
531   function technique and SH-wave and Love wave analysis are considerably improved after applying the
532   HPS noise reduction algorithm.

533   Group velocity analysis of teleseismic surface wavetrains showed that application of the HPS noise
534   reduction technique allows to analyze more events and to analyze them in a broader frequency range.
535   Especially more and wider Love wave dispersion curves could be recovered. The noise reduction algorithm
536   improves the horizontal components significantly, which allows the OBS community to apply a broader
537   range of seismological methodologies, including the horizontal components, to the OBS-data.

538   In conclusion, the presented method is a powerful algorithm for separation and extraction of different
539   signals from OBS data and has especially application in noise reduction of OBS signals.

540   **Code and data availability**

541   A Python package named NoiseCut (Zali, 2022) and the code related to the proposed method along with an
542   example of real data is freely available from https://github.com/ZahraZali/NoiseCut. The average
543   computation time for this example (one day OBS signal with a sampling frequency of 100 Hz) is about 7
544   minutes on a PC with an Intel core i7 (six-core) processor of 2.2 GHz and 16 GB of RAM. A Jupyter
545   notebook with all the Python codes and parameters related to the proposed method is available as an
546   electronic supplement. The sea floor seismological data were archived by Alfred Wegener Institute (AWI),
547   Helmholtz Centre for Polar Research, Bremerhaven, Germany, and are available upon request. The
548   supplementary material related to this article contains list of all earthquakes used in this study and a map
549   showing their location. The illustrations of the semi-synthetic data generation are presented in the

550 supplementary material as well. An example of three components seismogram and spectrogram before and

551 after applying HPS noise reduction algorithm to real data, Rayleigh wave group velocity analysis for a

552 synthetic example, MFT analysis for three real events and group velocity curves for some real events are

553 also presented through figures in the supplementary material.

554

555 **Author contribution**

556 Z.Z. developed the algorithm and designed the study. T.R. created the synthetics data, conducted the

557 synthetic tests, and measured the receiver functions. F.K. conducted the group velocity analysis. Z.Z., T.R.,

558 and F.K. evaluated the results. Z.Z. and T.R. wrote the initial draft. All authors wrote the final manuscript

559 and discussed the results.

560

561 **Competing interests**

562 The authors declare that they have no conflict of interest.

576

577 **References**

578 Alfred-Wegener-Institut, Helmholtz-Zentrum für Polar- und Meeresforschung et al.: DEPAS (Deutscher

579 Geräte-Pool für amphibische Seismologie): German Instrument Pool for Amphibian Seismology, J.

580 Largescale Res. Facil., 3, A122, https://doi.org/10.17815/jlsrf-3-165, 2017.

581

582 Ammon, C. J., Randall, G. E., & Zandt, G.: On the nonuniqueness of receiver function inversions, J.

583 Geophys. Res.-Sol. Ea., 95(B10), 15303-15318, https://doi.org/10.1029/JB095iB10p15303, 1990.

584

585 An, C., Cai, C., Zhou, L., & Yang, T.: Characteristics of Low-Frequency Horizontal Noise of Ocean-
586 Bottom Seismic Data, Seismol. Res. Lett., https://doi.org/10.1785/0220200349, 2021.
587

588 Bell, S. W., Forsyth, D. W., & Ruan, Y.: Removing noise from the vertical component records of ocean-
589 bottom seismometers: Results from year one of the Cascadia Initiative, B. Seismol. Soc. Am., 105(1), 300-
590 313, https://doi.org/10.1785/0120140054, 2015.
591

592 Beyreuther, M., Barsch, R., Krischer, L., Megies, T., Behr, Y., Wassermann, J.: ObsPy: A Python
593 Toolbox for Seismology. Seismol. Res. Lett., 81(3), 530-533, 2010.
594 Brink, K. H.: Tidal and lower frequency currents above Fieberling Guyot. J. Geophys. Res.-:
595 Oceans, 100(C6), 10817-10832, https://doi.org/10.1029/95JC00998, 1995.
596

597 Corela, C.: Ocean bottom seismic noise: applications for the crust knowledge, interaction ocean-
598 atmosphere and instrumental behaviour. Ph.D. thesis, University of Lisbon, 339 pp, 2014.
599

600 Crawford, W. C.: Determination of oceanic crustal shear velocity structure from seafloor compliance
601 measurements (Doctoral dissertation, University of California, San Diego), 1994.
602

603 Crawford, W. C., & Webb, S. C.: Identifying and removing tilt noise from low-frequency (< 0.1 Hz)
604 seafloor vertical seismic data. B. Seismol. Soc. Am., 90(4), 952-963, https://doi.org/10.1785/0119990121,
605 2000.
606

607 Crawford, W. C., Webb, S. C., & Hildebrand, J. A.: Estimating shear velocities in the oceanic crust from
608 compliance measurements by two-dimensional finite difference modeling. J. Geophys. Res.-Sol. Ea.,
609 103(B5), 9895-9916, https://doi.org/10.1029/97JB03532, 1998.
610

611 Deuss, A.: Global observations of mantle discontinuities using SS and PP precursors. Surv.
612 Geophys., 30(4-5), 301-326, https://doi.org/10.1007/s10712-009-9078-y, 2009.
613

614 Driedger, Jonathan, Meinard Müller, and Sascha Disch. "Extending Harmonic-Percussive Separation of
615 Audio Signals." In ISMIR, pp. 611-616. 2014.
616

617 Duennebier, F. K., & Sutton, G. H.: Fidelity of ocean bottom seismic observations, Oceanographic
618 Literature Review, 10(43), 996, https://doi.org/10.1007/BF01204343, 1995.
619

620 Dziewonski, A., S. Bloch, and M. Landisman.: A technique for the analysis of transient seismic signals, B.
621 Seismol. Soc. Am., 59, no. 1, 427-444, https://doi.org/10.1785/BSSA0590010427, 1969.

622

623 Essing, D., Schlindwein, V., Schmidt-Aursch, M. C., Hadziioannou, C., & Stähler, S. C.: Characteristics of

624 Current-Induced Harmonic Tremor Signals in Ocean-Bottom Seismometer Records, Seismol. Res.

625 Lett., 92(5), 3100-3112. , https://doi.org/10.1785/0220200397, 2021.

626

627 Eulenfeld, T.: rf: Receiver function calculation in seismology, Journal of Open Source Software, 5(48),

628 1808, https://doi.org/10.21105/joss.01808, 2020.

629

630 Fitzgerald, D.: Harmonic/percussive separation using median filtering, In Proceedings of the International

631 Conference on Digital Audio Effects (DAFx) (Vol. 13), 2010.

632

633 FitzGerald, D.: Vocal separation using nearest neighbours and median filtering, 23rd IET Irish Signals and

634 Systems Conference, Maynooth. 28-29th. June 2012, https://doi.org/10.1049/ic.2012.0225, 2012.

635

636 Friedrich, A., Krüger, F., & Klinge, K.: Ocean-generated microseismic noise located with the Gräfenberg
637 array, J. Seismol., 2(1), 47-64, https://doi.org/10.1023/A:1009788904007, 1998.
638

639 Gaspà Rebull, O., Cusí, J. D., Ruiz Fernández, M., & Muset, J. G.: Tracking fin whale calls offshore the

640 Galicia Margin, north east Atlantic Ocean, The Journal of the Acoustical Society of America, 120(4), 2077-

641 2085, https://doi.org/10.1121/1.2336751, 2006.

642

643 Griffin, O. M.: Vortex-Induced Vibrations of Marine Cables and Structures, NRL Memorandum Report

644 5600, Naval Research Laboratory – Marine Technology Division, Washington D.C, 1985.

645

646 Hannemann, K., Krüger, F., Dahm, T., & Lange, D.: Structure of the oceanic lithosphere and upper mantle

647 north of the Gloria fault in the eastern mid-Atlantic by receiver function analysis, J. Geophys. Res-Sol Ea.,

648 122(10), 7927-7950, https://doi.org/10.1002/2016JB013582, 2017.

649

650 Hasselmann, K.: A statistical analysis of the generation of microseisms. Rev. Geophys., 1(2), 177-210,

651 https://doi.org/10.1029/RG001i002p00177, 1963.

652

653 Heimann, S., Kriegerowski, M., Isken, M., Cesca, S., Daout, S., Grigoli, F., Juretzek, C., Megies, T.,

654 Nooshiri, N., Steinberg, A., Sudhaus, H., Vasyura-Bathke, H., Willey, T., Dahm, T.: Pyrocko - An open-

655 source seismology toolbox and library. V. 0.3. GFZ Data Services,

656 https://doi.org/10.5880/GFZ.2.1.2017.001, 2017.

657

658 Herrmann, R. B.: Computer programs in seismology: An evolving tool for instruction and research, Seism.

659 Res. Lettr., 84, 1081-1088, https://doi.org/10.1785/0220110096, 2013.

660

661 Janiszewski, H. A., Gaherty, J. B., Abers, G. A., Gao, H., & Eilon, Z. C.: Amphibious surface-wave phase-
662 velocity measurements of the Cascadia subduction zone. Geophys. J. Int., 217(3), 1929-1948,
663 https://doi.org/10.1093/gji/ggz051, 2019.

664

665 Johnson, J. B., & Watson, L. M.: Monitoring volcanic craters with infrasound "music", Eos, 100.
666 https://doi.org/10.1029/2019EO123979, 2019.

667

668 Kennett, B. L., Engdahl, E. R., & Buland, R.: Constraints on seismic velocities in the Earth from
669 traveltimes. Geophys. J. Int., 122(1), 108-124, https://doi.org/10.1111/j.1365-246X.1995.tb03540.x, 1995.

670

671 Kind, R., Kosarev, G. L., & Petersen, N. V.: Receiver functions at the stations of the German Regional
672 Seismic Network (GRSN). Geophys. J. Int., 121(1), 191-202, https://doi.org/10.1111/j.1365-
673 246X.1995.tb03520.x, 1995.

674

675 Langston, C.A.: Structure under Mount Rainier, Washington, inferred from teleseismic body waves. J.
676 Geophys. Res., 84, 4749-4762, https://doi.org/10.1029/JB084iB09p04749, 1979.

677

678 Ligorría, J. P., & Ammon, C. J.: Iterative deconvolution and receiver-function estimation. B. Seismol. Soc.
679 Am., 89(5), 1395-1400, https://doi.org/10.1785/BSSA0890051395, 1999.

680

681 Longuet-Higgins, M. S.: A theory of the origin of microseisms, Philosophical Transactions of the Royal
682 Society of London. Series A, Mathematical and Physical Sciences, 243(857), 1-35,
683 https://doi.org/10.1098/rsta.1950.0012, 1950.

684

685 McFee, B., V. Lostanlen, A. Metsai, M. McVicar, S. Balke, C. Thomé, C. Raffel, F. Zalkow, A. Malek,
686 Dana, et al.: librosa/librosa: 0.8.0, Version 0.8.0, Zenodo, https://doi.org/10.5281/zenodo.3955228, 2020.

687

688 Mousavi, S. M., & Langston, C.A.: Automatic noise-removal/signal-removal based on general cross-
689 validation thresholding in synchrosqueezed domain and its application on earthquake data. Geophysics,
690 82.4, V211-V227. https://doi.org/10.1190/geo2016-0433.1, 2017.

691

692 Müller, M.: Fundamentals of music processing: Audio, analysis, algorithms, applications. Cham,
693 Switzerland: Springer International Publishing. https://doi.org/10.1007/978-3-319-21945-5, 2015.

694

695 Negi, S. S., Kumar, A., Ningthoujam, L. S., & Pandey, D. K.: An Efficient Approach of Data Adaptive
696 Polarization Filter to Extract Teleseismic Phases from the Ocean-Bottom Seismograms. Seismological
697 Society of America, 92(1), 528-542, https://doi.org/10.1785/0220200034, 2021.

699 Olofsson, B.: Marine ambient seismic noise in the frequency range 1–10 Hz. The Leading Edge, 29(4),
700 418-435, https://doi.org/10.1190/1.3378306, 2010.

702 Pereira, A., Romagosa, M., Corela, C., Silva, M. A., & Matias, L.: Source Levels of 20 Hz Fin Whale
703 Notes Measured as Sound Pressure and Particle Velocity from Ocean-Bottom Seismometers in the North
704 Atlantic. Journal of Marine Science and Engineering, 9(6), 646, https://doi.org/10.3390/jmse9060646,
705 2021.

707 Pillet, R., Deschamps, A., Legrand, D., Virieux, J., Béthoux, N., & Yates, B.: Interpretation of broadband
708 ocean-bottom seismometer horizontal data seismic background noise, B. Seismol. Soc. Am., 99(2B), 1333-
709 1342, https://doi.org/10.1785/0120080123, 2009.

711 Rafii, Z., Liutkus, A., & Pardo, B.: REPET for background/foreground separation in audio. In Blind Source
712 Separation (pp. 395-411). Springer, Berlin, Heidelberg, https://doi.org/10.1007/978-3-642-55016-4_14,
713 2014.

715 Rafii, Z., Liutkus, A., Stöter, F. R., Mimilakis, S. I., FitzGerald, D., & Pardo, B.: An overview of lead and
716 accompaniment separation in music, IEEE/ACM Transactions on Audio, Speech, and Language
717 Processing, 26(8), 1307-1335. https://doi.org/10.1109/TASLP.2018.2825440, 2018.

719 Rafii, Z., & Pardo, B.: Music/Voice Separation Using the Similarity Matrix, Proc. ISMIR, pp. 583-588,
720 2012.

722 Ramakrushana Reddy, T., Dewangan, P., Arya, L., Singha, P., & Kamesh Raju, K. A.: Tidal triggering of
723 the harmonic noise in ocean-bottom seismometers. Seismol. Res. Lett., 91(2A), 803-813,
724 https://doi.org/10.1785/0220190080, 2020.

726 Rondenay, S.: Upper mantle imaging with array recordings of converted and scattered teleseismic waves.
727 Surv. Geophys., 30(4), 377-405, https://doi.org/10.1007/s10712-009-9071-5, 2009.

729 Romanowicz, B., Stakes, D., Montagner, J. P., Tarits, P., Uhrhammer, R., Begnaud, M., Stutzmann, E.,
730 Pasyanos, M., Karczewski, J.F., Etchemendy, S. and Neuhauser, D.: MOISE: A pilot experiment towards

731 long term sea-floor geophysical observatories, Earth, planets and space, 50(11), 927-937,

732 https://doi.org/10.1186/BF03352188, 1998.

733

734 Schlindwein, V., Krüger, F., Schmidt-Aursch, M.: Project KNIPAS: DEPAS ocean-bottom seismometer

735 operations in the Greenland Sea in 2016-2017, Alfred Wegener Institute, Helmholtz Centre for Polar and

736 Marine Research, Bremerhaven, PANGAEA, https://doi.org/10.1594/PANGAEA.896635, 2018.

737

738 Schlindwein, V., Wassermann, J., & Scherbaum, F.: Spectral analysis of harmonic tremor signals at Mt.

739 Semeru volcano, Indonesia, Geophys. Res. Lett., 22(13), 1685-1688. https://doi.org/10.1029/95GL01433,

740 1995.

741

742 Skop, R. A., & Griffin, O. M.: On a theory for the vortex-excited oscillations of flexible cylindrical

743 structures. Journal of Sound and Vibration, 41(3), 263-274, https://doi.org/10.1016/S0022-460X(75)80173-

744 8, 1975.

745

746 Silver, P.G. & Chan, W.W.: Shear wave splitting and subcontinental mantle deformation. J. Geophys. Res.,

747 96, 16429-16454, https://doi.org/10.1029/91JB00899, 1991.

748

749 Snodgrass, F. E., Hasselmann, K. F., Miller, G. R., Munk, W. H., & Powers, W. H.: Propagation of ocean

750 swell across the Pacific, Philosophical Transactions of the Royal Society of London. Series A,

751 Mathematical and Physical Sciences, 259(1103), 431-497, https://doi.org/10.1098/rsta.1966.0022, 1996.

752

753 Stähler, S. C., Schmidt-Aursch, M. C., Hein, G., & Mars, R.: A self-noise model for the German DEPAS

754 OBS pool. Seismol. Res. Lett., 89(5), 1838-1845, https://doi.org/10.1785/0220180056, 2018.

755

756 Tanimoto, T., Rivera, L.: The ZH ratio method for long-period seismic data: sensitivity kernels and

757 observational techniques. Geophys. J. Int., 172(1), 187-198, https://doi.org/10.1111/j.1365-

758 246X.2007.03609.x, 2008.

759

760 Titze, I. R.: Nonlinear source–filter coupling in phonation: Theory, The Journal of the Acoustical Society

761 of America, 123(4), 1902-1915, https://doi.org/10.1121/1.2832337, 2008.

762

763 Vaseghi, S. V.: Advanced signal processing and digital noise reduction. Vieweg + Teubner Verlag,

764 https://doi.org/10.1002/9780470740156, 1996.

765

766 Wang, R.: A simple orthonormalization method for stable and efficient computation of Green's

767 functions, B. Seismol. Soc. Am., 89(3), 733-741, https://doi.org/10.1785/BSSA0890030733, 1999.

768

769 Webb, S. C.: Broadband seismology and noise under the ocean, Rev. Geophys., 36(1), 105-142,

770 https://doi.org/10.1029/97RG02287, 1998.

771

772 Webb, S. C., Zhang, X., & Crawford, W.: Infragravity waves in the deep ocean, J. Geophys. Res.-:

773 Oceans, 96(C2), 2723-2736, https://doi.org/10.1029/90JC02212, 1991.

774

775 Zahra Zali. (2022). ZahraZali/NoiseCut: NoiseCut (v1.0.0). Zenodo.

776 https://doi.org/10.5281/zenodo.7339552

777

778 Zali, Z., Ohrnberger, M., Scherbaum, F., Cotton, F., & Eibl, E. P.: Volcanic Tremor Extraction and

779 Earthquake Detection Using Music Information Retrieval Algorithms, Seismol. Res. Lett., 92(6), 3668-

780 3681, https://doi.org/10.1785/0220210016, 2021.

781

782 Zhu, W., Mousavi, S. M., & Beroza, G. C.: Seismic signal denoising and decomposition using deep neural

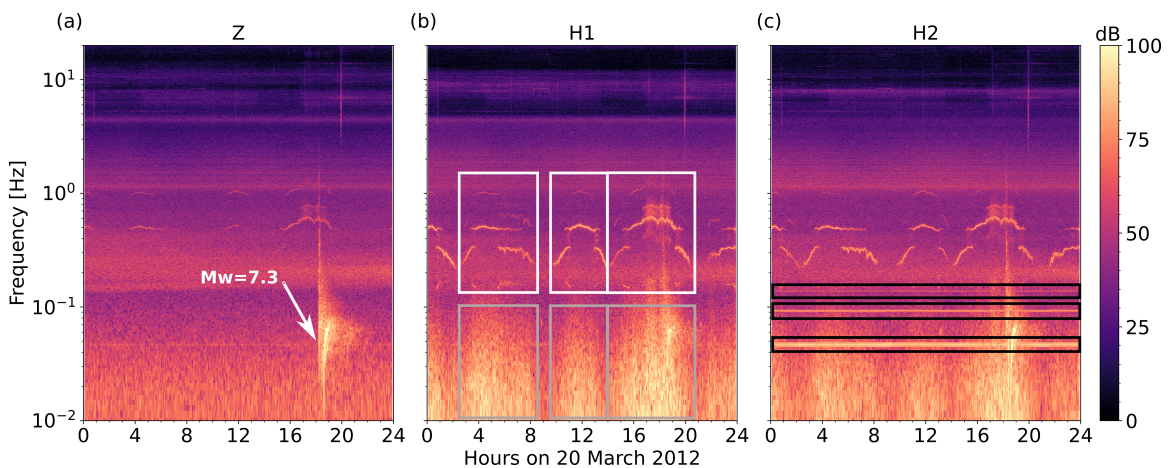783 networks. IEEE T. Geosci. Remote., 57(11), 9476-9488. https://doi.org/10.1109/TGRS.2019.2926772,

784 2019.

785

786

787

788
789

790 **Figure 1: Spectrogram of an one-day OBS signal shows ocean bottom noise on Z (a), H1 (b) and H2 (c)**

791 **components. The data was recorded by the station D10 of the DOCTAR array with a sampling frequency of 100**

792 **Hz. The spectrogram were calculated using a window length of 2^{16} sample and an overlap of 75%. The signal**

793 **of an earthquake (Mw=7.3) on 20.3.2012 at around 18:00 at the station D10 is shown in (a). The tidal cycle of**

the current-induced noise is clearly visible during the high tilt noise episodes (grey box in b). The white box in (b) highlights the tremor episodes caused by the head buoy strumming. On H2 (c) we see an instrument-related, presumably electronic noise (black boxes). The high energy of the secondary microseism band at around 0.2 Hz is visible on all components.
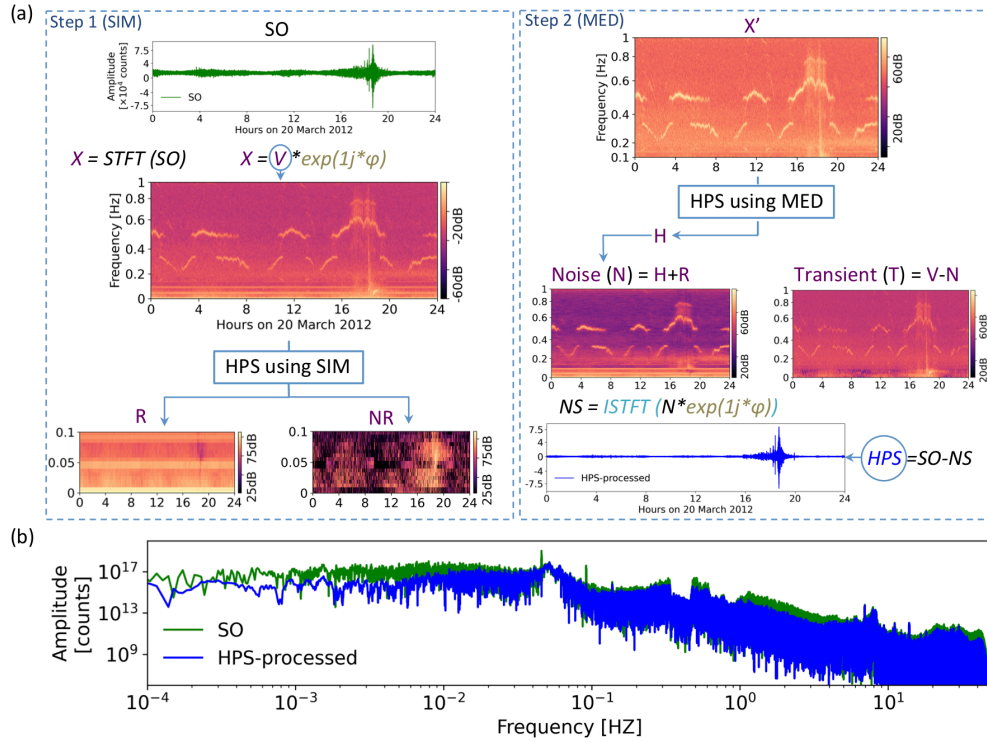

Figure 2: Method flowchart (a) Illustration of the processing steps with a real data example. Left panel shows the first step of the method where using the similarity matrix (SIM) in the frequency range below 0.1 Hz and above 1 Hz, we divide the spectrogram (X) of the original signal (SO) into two spectrograms of repeating (R) and non-repeating (NR) patterns. Right panel shows the second step of the method where we apply a median filter (MED) to the frequency range of 0.1 to 1 Hz (spectrogram X') in order to remove noises from this frequency range. It results in the harmonic spectrogram (H). As the interested frequency range for OBS signals is below 1 Hz, the spectrograms show only this frequency range. Finally the noise spectrogram (N) is created by summing the separated noises derived from two steps and the noise signal (NS) is derived using ISTFT. We obtain the noise reduced signal (HPS) by subtracting the NS from the input OBS signal (SO). STFT, short time Fourier transform. HPS, harmonic-percussive separation. SIM, similarity matrix. MED, median filtering. ISTFT, Inverse Short Time Fourier Transform. (b) Spectrum of the original signal (SO) and the HPS noise reduced signal.
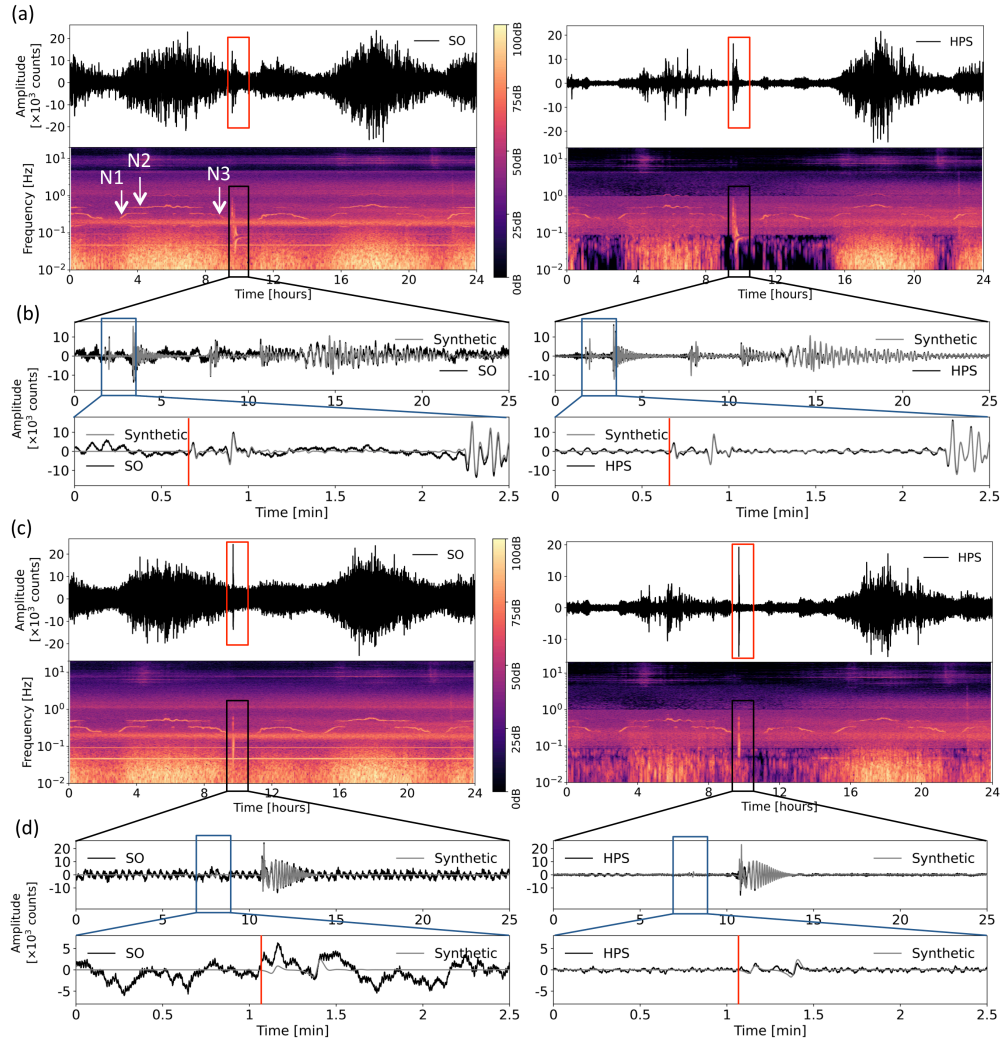
815

Figure 3: Comparison of the synthetic seismograms and spectrograms of the original signal SO and the HPS noise reduced signal on the R and T components for a synthetic signal with SNR= 1.5 before denoising. (a) & (c) Show one day seismograms and spectrograms for R and T components, respectively. Squares show the earthquake section. The arrows in (a) show three noise situations (N1-N3). (b) & (d) Show seismograms of the earthquake section on SO and HPS signals, with detailed view of the P-arrival (on component R in subfigure b) and SH-arrival (on component T in subfigure d). Red lines show P-arrivals in (b) and SH-arrival in (d).
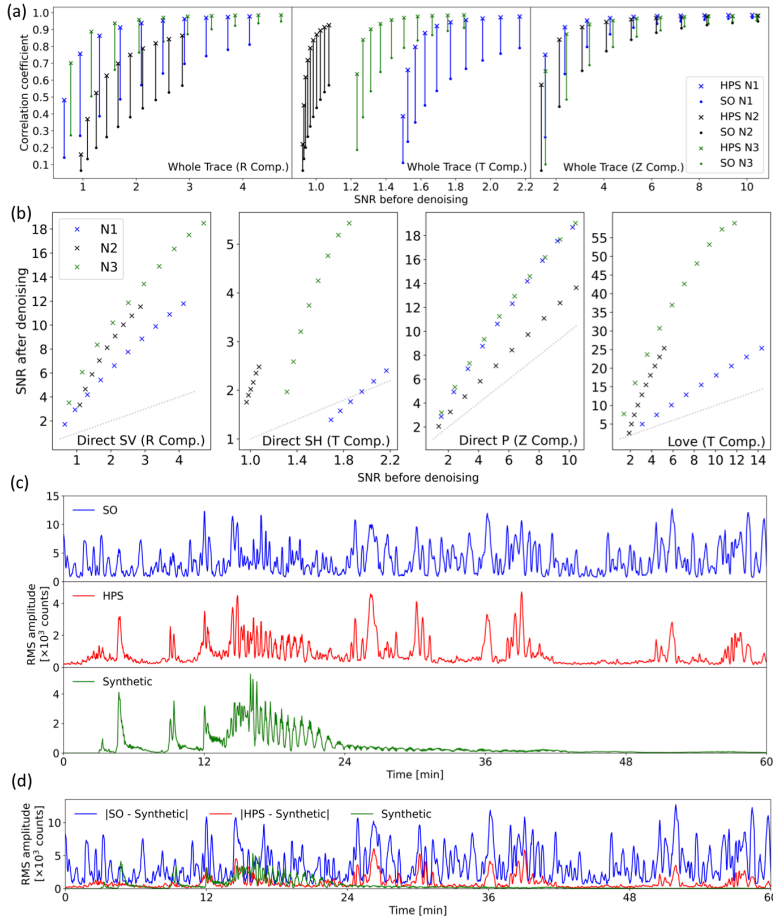
822

Figure 4: Comparison of the synthetic SO and HPS signals (both are lowpass filtered at 1Hz). (a) Correlation coefficients (for the whole trace) for different SNRs and 3 realistic noise realizations for Z, R and T components (Component is abbreviated as Comp.). (b) Improvement of SNR for direct body wave phases and the Love wave. The gray dotted lines in (b) mark the line with gradient 1 (no improvement of SNR). (c) Comparison of the root mean square (RMS) amplitude of one example of the SO, HPS and synthetic earthquake signals. This signal is the same example shown in Fig. 3 (R component, SNR= 1.5 before denoising). (d) The RMS of the original noise (blue trace: |SO - Synthetic|) and the remained noise after denoising (red trace: |HPS- Synthetic|) compared to the synthetic earthquake signal.
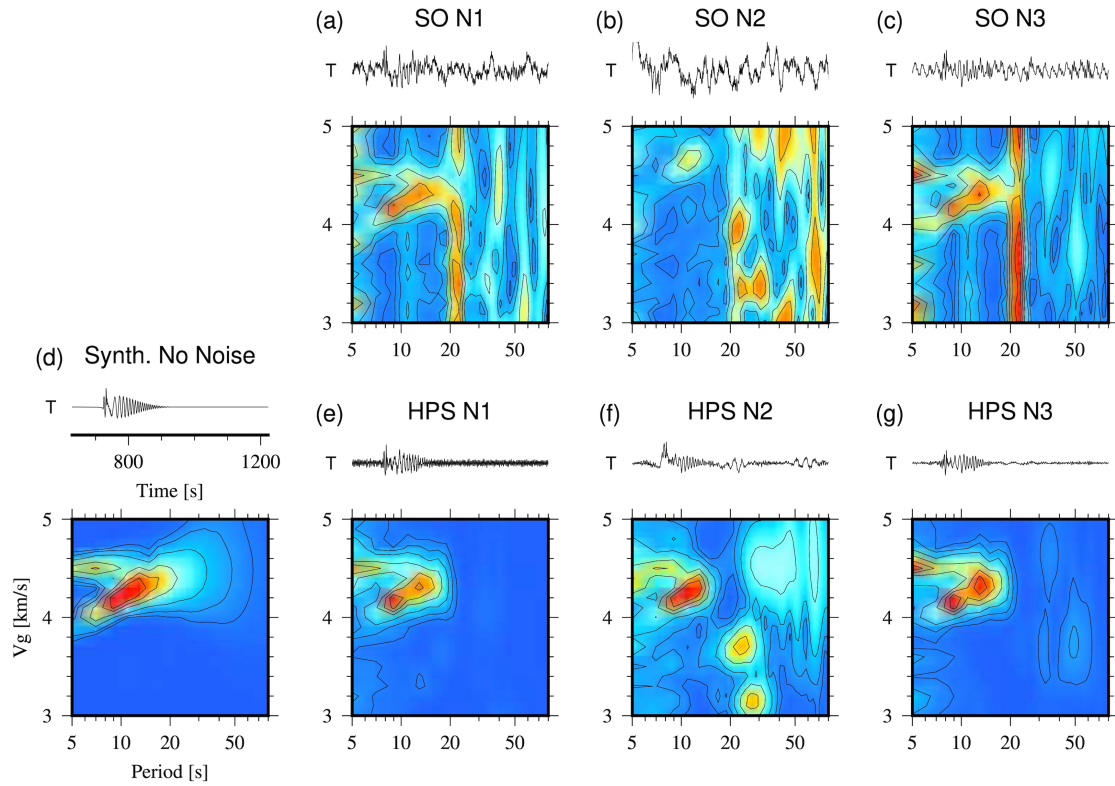
26

Figure 5: Love wave group velocity analysis for unfiltered and HPS processed synthetic Love wavetrains contaminated by three real world OBS noise signals (noise situations N1-N3, station D10, DOCTAR experiment, see Sect. 2 for more details). (a)–(c): Lower panels: Unfiltered synthetic signal (SO) MFT analysis results. Top panels: seismogram time windows corresponding to the range of group velocities shown on the y-axis. (d) Noise free synthetic case. (e)–(g): HPS processed input traces for noise situations N1-N3 (lower panel: MFT analysis result, top panel: HPS processed seismogram).
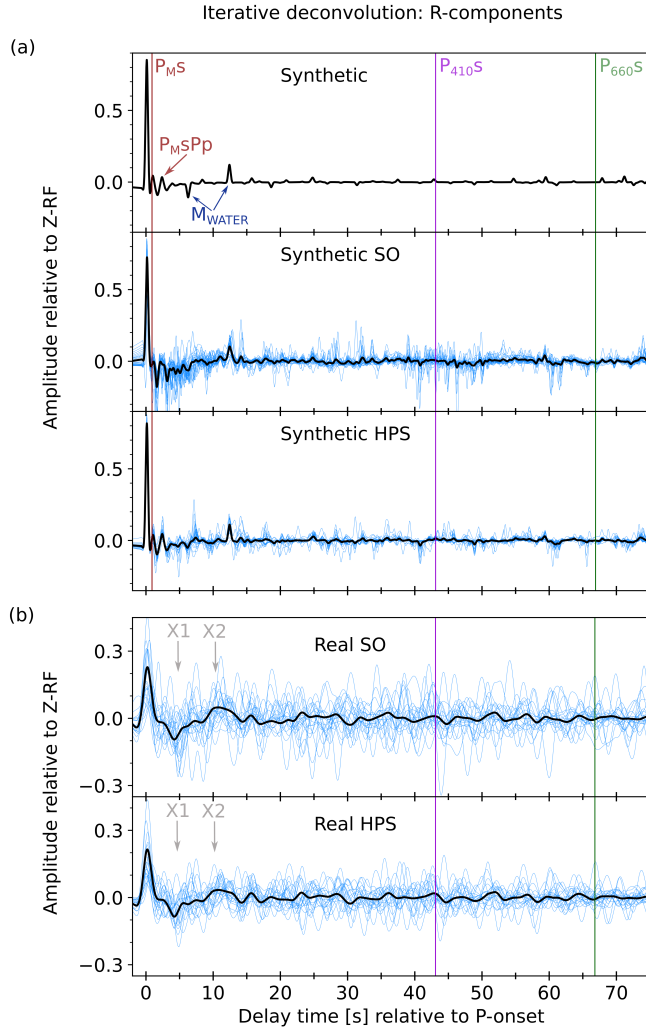
Figure 6: R-receiver function comparison of synthetic and real data examples. (a) Comparison of the synthetic data examples, lowpass filtered at 2 Hz. The pure synthetic R-RF is shown in the uppermost panel, followed by the synthetic SO and the synthetic HPS R-RFs. The black lines show the summed individual R-RFs (blue waveforms). The theoretical onset times for this specific model are marked. Red line: Ps-arrival of the Moho (P_MS) and its multiple (P_MsPp), violet line: Ps arrival of the 410 ($P_{410}s$), green line: Ps-arrival of the 660 ($P_{660}s$), dark-blue arrows: Multiples in the watercolumn of 4.9 km (M_{WATER}), repetitive every 6.5s. **(b)** Comparison of the real data, bandpass filtered at 0.05–0.5 Hz. The upper panel shows the R-RFs of the real SO traces and the lowermost panel the R-RFS of the real HPS traces. The individual traces (blue) are shown as stack (black line) and the theoretical onset times based on the average ak135 velocity model are shown as violet line ($P_{410}s$) and green line ($P_{660}s$). The origin of the phases X1 and X2 (grey) remain unclarified, since their interpretation is beyond the scope of this study.

854 **Table 1: Parameters values used in our study**

Parameters	Frequency range for SIM	Frequency range for MED	FFT window size	FFT overlapping percentage	Waiting factor in SIM	Kernel size in MED
Values	[0-0.1] & above 1 Hz	[0.1-1] Hz	16384 samples	75%	2 hours	80

855